Comprehensive Comparison of Continuous-Wave and Linear-Frequency-Modulated Continuous-Wave Radars for Short-Range Vital Sign Monitoring

Elías Antolinos, *Student Member, IEEE*, and Jesús Grajal, *Senior Member, IEEE*

***Abstract*—The use of radar technology for contactless monitoring of cardiorespiratory activity has been a significant research topic for the last two decades. However, despite the abundant literature focusing on the use of different radar architectures for healthcare applications, an in-depth analysis is missing about the most appropriate configuration. This article presents a comparison between continuous-wave (CW) and linear-frequency-modulated continuous-wave (LFMCW) radars for application in vital sign monitoring scenarios. These waveforms are generated with the same architecture at two different frequencies: 24 and 134 GHz. Results evidence that both configurations are capable of measuring general metrics, such as the breathing and heart rates. However, LFMCW offers better results in the identification of cardiac events and the extraction of certain derived biomarkers, such as the heart rate variability sequences (HRV). Conclusions show that this performance does not depend on the selected working frequency.**

***Index Terms*—CW radar, HRV sequence, LFMCW radar, vital sign monitoring.**

I. Introduction

THE fields of application of radar technology have significantly increased since the first patent registration in 1904, when Christian Hülsmeyer registered a method for reporting distant metallic objects using electric waves [1]. The origin of radar and its main application area was typically military due to their high costs and bulky sizes. Nevertheless, advances on monolithic microwave integrated circuits (MMIC) have allowed radar systems to be miniaturized and easily integrated into any device [2], [3]. Therefore, they can be currently found in diverse environments such as automotive [4], security [5], industrial [6], structure-health monitoring [7], and even, in biomedical and healthcare contexts [8], [9].

Manuscript received 2 February 2023; revised 3 March 2023; accepted 10 March 2023. Date of publication 16 March 2023; date of current version 19 May 2023. The work of Elías Antolinos was supported by an FPU Fellowship granted by the Spanish Ministry of Education under Grant FPU18/01525. This work was supported by the Spanish Ministry of Science and Innovation under Project PID2020-113979RB-C21 (MCIN/AEI/10.13039/501100011033). This paper was recommended by Associate Editor N. McFarlane. *(Corresponding author: Elías Antolinos.)*

The authors are with the Information Processing and Telecommunications Center, Universidad Politécnica de Madrid, 28040 Madrid, Spain (e-mail: elias.antolinos@upm.es).

Color versions of one or more figures in this article are available at https://doi.org/10.1109/TBCAS.2023.3257647.

Digital Object Identifier 10.1109/TBCAS.2023.3257647

Regarding the biomedical field, non-contact monitoring of human vital signs with radar has become an active research area in recent years [10]. Throughout these years, radars have been exploited to measure the chest's wall displacement due to the breathing and heart movements. The nature of the radar signal acquired is mechanical. Therefore, this makes difficult its direct comparison with the standard reference used in cardiac monitoring, the electrocardiogram (ECG), which measures electrical activity. Thus, some authors have compared the radar signal acquired with references providing mechanical information, such as seismocardiograms (SCG) [11] -which measure accelerations-, impedance cardiograms (ICG) [12] -which measure the thoracic impedance-, or phonocardiographs (PCG) [13] -which measure sound waves derived from the heart movements. In these studies, authors coincide in the fact that the radar signal acquired is highly correlated with vibrations derived from the volume and pressure changes. Due to this fact, the radar is capable of detecting certain characteristic heart events, for instance, the opening and closing of the different valves. These events are used in the extraction of some important biomarkers, such as the heart rate variability (HRV), which have a demonstrated clinical significance in the diagnosis of several cardiovascular diseases [14].

Among the most used radar configurations for cardiopulmonary monitoring, it stands out the Doppler or continuous-wave (CW) radar [15], [16], the linear-frequency-modulated continuous-wave (LFMCW) radar [17], [18] and the impulse radar [19]. The use of impulse radar is not as extended due to its high power requirements and more complex system architecture [20].

Although there is an extensive bibliography focusing on the comparison between CW and LFMCW radars for healthcare applications [20], [21], [22], [23], [24], it is not clear which radar configuration offers the best solution. A qualitative comparison of mono- and multi-mode architectures for short-range continuous-wave radars is presented in [20], where they state that CW radars have a higher sensitivity to small vibrations than LFMCW radars, while LFMCW configuration allows the separation of echoes from different targets, but they do not provide a quantitative comparison of both configurations. On the other hand, it is highlighted in [25] that LFMCW radars are not as efficient as CW radars because they needs to sample the target position at higher frequencies than the fundamental

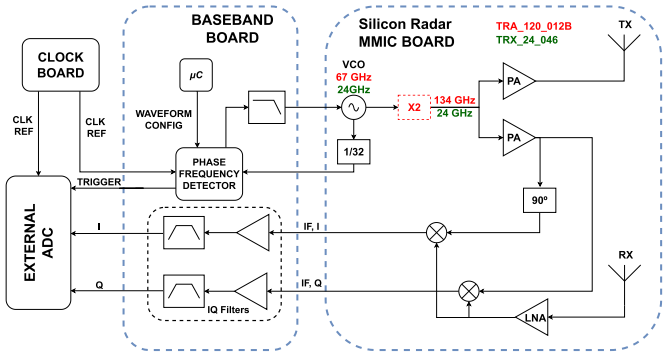

Fig. 1. Diagram of the radar's RF and baseband architecture. The baseband board is common for both frequencies: 24 and 134 GHz. The architecture differences between the MMIC boards are represented in red, for the 134 GHz radar, and in green, for the 24 GHz radar.

vibration frequency to be measured, but they go no further in this comparison. However, recent advances in technology bring solutions to these issues. For instance, low-cost commercial microcontrollers embed analog-to-digital converters that can operate at sampling frequencies in the range of 5–10 MS/s, with resolution of 12–16 bits. With these microcontrollers and typical configurations in LFMCW radars, such as sweep time of 1 ms and bandwdith of 3 GHz, these radars can measure targets up to 250 m. Thus, sampling frequency is not longer a limitation in selecting the best radar configuration for vital sign monitoring.

This paper presents a comparison between CW and LFMCW radars to determine which one suits better for vital sign monitoring. In order to perform this comparison, a commercial baseband board from a 134 GHz radar has been modified to operate indistinctly in CW or LFMCW configurations. This modifications allow to use the same baseband board with two different front-ends: one at 134 GHz and other at 24 GHz, as shown in Fig. 1. The analysis is carried out at 134 GHz and the findings are confirmed with the 24 GHz radar.

The radar working frequencies have not been chosen arbitrarily. Firstly, increasing the working frequency enhances the measurement accuracy, since, at high frequencies, small displacements result in significant phase changes, as is shown in Section II. Moreover, working at higher frequencies results in more compact devices. It allows to reduce antenna sizes and to get narrower beamwidths. On the other hand, higher frequencies experience more attenuation. However, radar based short-distance applications are not usually power limited, so high attenuation is not considered a limitation. Additionally, the dielectric properties of the human body tissues have been estimated along the millimeter-wave band [26], where it was concluded that the reflection from the body tissues is stronger at higher frequencies, since the complex dielectric constant decreases with frequency.

The performance of both configurations have been tested in two different scenarios. The first one is a controlled scenario where the periodic displacements of the membrane of a woofer are measured. In the second scenario, the radars acquire the cardiorespiratory activity of a person by analysing his chest displacement. In this scenario, the radar signal is captured simultaneously by two radars: one radar operating in CW and the other one in LFMCW. The extracted vital signs are compared with a reference ECG provided by the Task Force Monitor, a clinically tested reference from CNSystems [27].

The rest of the paper is organized as follows. Section II details the CW and LFMCW radar working principles, the signal processing algorithms to extract the desired signals and the metrics used to perform the comparison between both operation configurations. Section III details the different signals that can be obtained from the radar signal. Finally, results are presented and discussed in Section IV, and conclusions are drawn in Section V.

II. Background

A. Hardware

This section details the hardware setup used in this study, which is composed by three different pieces of equipment:

- The radar sensor. The modifications of a commercial radar sensor are presented.
- The SCG is the main reference used in this work, since it also provides mechanical information.
- The Task Force Monitor (TFM), which provides an additional reference with ECGs.

1) Radar Sensor: The radar sensors used are based on a LFMCW radar fabricated by Silicon Radar [28]. In order to better fit the desired application, the commercial version of the radar baseband board has been modified. This modifications allows to use the radar sensor at two frequencies (24 and 134 GHz) only by exchanging the MMIC board, and in CW or LFMCW configurations. The main modifications have been the replacement of the commercial radar's microcontroller and baseband boards with custom-made PCBs. The system architecture is common for both operating configurations, and its diagram is presented in Fig. 1. The radar system consists of:

- A commercial MMIC board fabricated by Silicon Radar. In this work, two MMIC boards have been used, one operating at 134 GHz and the other at 24 GHz. The difference in architecture between both boards is indicated in Fig. 1, each board has its specific VCO. In the 134 GHz board, the VCO frequency is 67 GHz and it is doubled to 134 GHz.
- A baseband board, which controls the MMIC, amplifies and filters the I/Q signals. This board includes the microcontroller (μC), the Phase Frequency Detector (PFD) and the I/Q filters:
  - The PFD used is the ADF4159 from Analog Devices. It can be configured to perform a frequency sweep, controlling the swept bandwidth, the duration and the linearity of the frequency sweep. Thus, it allows to configure the transmitted waveform, and, therefore, if the radar is operating in CW or LFMCW configuration withouth changing the hardware architecture. The reference oscillator used to feed the PDF has also been replaced by a new one, which is located in the clock board described below, that provides less phase noise, improving the dynamic range.

TABLE I
MAIN CHARACTERISTICS OF THE RADAR MODULES USED

Characteristic	Radar 134 GHz	Radar 24 GHz
Model	*TRA_120_012B*	*TRX_024_046*
Central Frequency (GHz)	134	24.6
Output Power (dBm)[1]	−3	4
Bandwidth (GHz)	16 (max)	3.6 (max)
Sweep Time	12 μs to 18 ms	12 μs to 18 ms
Sampling frequency	10 MHz	10 MHz
Antenna type	Dipole	6x4 Patch array
Beamwidth	15°(E) 40°(H)	25°(E) 15°(H)
Antenna Gain	6 dB	16 dB
Beamwidth (with the lens)[2]	4°(E) 4°(H)	-
Lens Gain	12 dB	-
Board dimensions (cm)	5x5	8x5

[1] Without antennas.
[2] The use of dielectric lens allows a narrower focusing. Lens are only used with the 134 GHz radar.

  - The commercial microcontroller has been replaced by the Attiny-167, a 8-bits microcontroller with 14 GPIO pins available. The commercial LFMCW radar's transmission was limited to intervals managed by its microcontroller. These intervals included off-time between clusters of LFMCW sweeps to allow for on-board signal processing and USB-to-PC data transmission, which would hinder continuous cardiopulmonary measurements. In this version all processing is offloaded to a PC, allowing continuous LFMCW operation.
  - I/Q filters. The analog filters applied to the in-phase and quadrature signals have been modified to be low-pass filters, allowing CW configuration. The cut-off frequency is 2 MHz.
- A clock board distributes the clock reference. The reference oscillator allocated in this board is a 80 MHz oscillator from the ABLNO series, from ABRACOM. This frequency can be divided with a programmable divider by powers of 2 from 2 to 16. Thus, the ADC sampling frequency can vary from 5 MHz to 80 MHz.
- An external ADC. The external ADC used is the model PCI-9846 from ADLINK, with 16 bits, 4 channels, and a configurable sampling frequency up to 40 MS/s.

More information about the hardware architecture, and the modifications carried out, can be found in [29]. The main radar characteristics are summarized in Table I, the system architecture can be found in Fig. 1 and a photograph of the radar modules can be seen in Fig. 2.

Unless otherwise stated, the results of this work have been obtained using the 134 GHz radar. The results at 24 GHz are only presented when explicitly indicated.

2) Seismocardiogram: The device is the ADXL335 from Analog Devices [30]. This sensor can measure the static acceleration of gravity and the dynamic acceleration resulting from motion or vibration. It is a 3-axis accelerometer, with a full sensing range of $\pm 3\,g$ and a sensitivity of 300 mV/g. For this analysis, only the normal axis to the surface is analyzed, which corresponds to the movement direction acquired with the radar. Moreover, the ADXL335 has an analog low-pass filter with a cut-off frequency of 50 Hz for the SCG output signal.

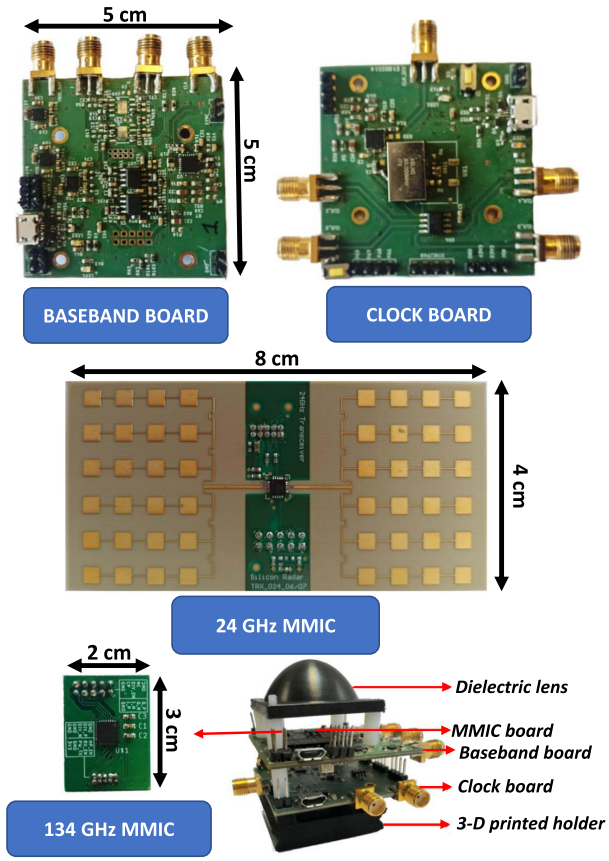

Fig. 2. Boards for the 134 and 24 GHz radars. From top to bottom: the baseband and clock boards, which are common for both frequencies, the 24 GHz MMIC board. At the bottom: the 134 GHZ MMIC board and a photograph of the 134 GHz radar global assembly with the MMIC located below the dielectric lens.

3) Task Force Monitor: The Task Force Monitor (TFM) developed by CNSystems [27] is used as an additional reference for the vital signs, since it can synchronously measure electrocardiogram (ECG), blood pressure (BP) and impedance cardiogram (ICG). The radar sensor and the TFM are synchronized using a gold-code sequence [31], which is generated in the clock board. For this analysis, only the ECG signal is used.

B. Working Operation Principles

This section introduces the basic principles of CW and LFMCW radars.

1) CW Radar: Non modulated CW radars transmit and receive a sinusoidal waveform of frequency f_o. After the demodulation and filtering processes, the radar baseband signal can be expressed as:

$$s_b(t) = \sigma \exp(j\phi(t)) \tag{1}$$

where σ is the signal amplitude, and $\phi(t) = \frac{4\pi f_o}{c} R(t)$. Being c, the light velocity; and $R(t)$, the target range.

2) LFMCW Radar: The working principle of LFMCW is based on transmitting a linear modulated RF signal, whic h is reflected by the target. A replica of the transmitted signal is mixed with the received echoes, obtaining the beat signal. Under

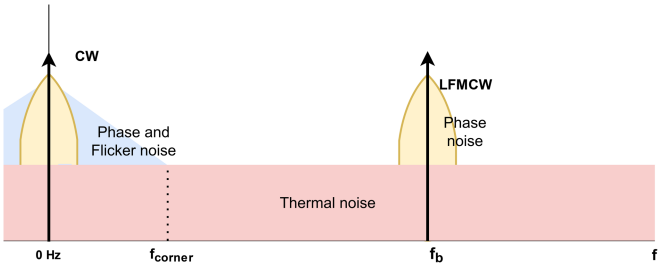

Fig. 3. Noise impact on CW and LFMCW configurations. It shows the main sources of noise affecting a radar system: thermal noise, phase noise and flicker noise.

the "stop and go assumption" [32], which states that the target does not change its position during the radar sweep time, the beat signal for a point-scatterer at a range $R(\tau)$ (where τ is the so-called slow time [1])can be formulated as:

$$s_b(t,\tau) = \sigma \exp(j(2\pi f_b(\tau)t + \phi(\tau) + \phi_2(\tau))) \tag{2}$$

The beat signal follows a sinusoidal waveform with a frequency known as beat frequency $f_b(\tau) = \frac{2B}{T \cdot c} R(\tau)$, $\phi(\tau) = 4\pi f_c R(\tau)/c$, and $\phi_2(\tau) = -\frac{4\pi B R^2(\tau)}{T \cdot c^2}$, where f_c is the central frequency, B is the bandwidth, and T is the sweep time. $\phi_2(\tau)$ represents the residual video phase (RVP) [32], which is found to be negligible and can be ignored, since it is proportional to $1/c^2$.

From the previous equations, $f_b(\tau)$ is used for target location, enabling person separation in multi-target scenarios and removing unwanted interferences from clutter [33]. This target separation is carried out with a digital filter bank, implemented with an FFT (Fast Fourier Transform). On the other hand, $\phi(\tau)$ is used to extract the information relative to the target range. Moreover, as has been previously explained, a high operation frequency is selected for the central frequency to increase its sensitivity to small displacements, ΔR: $\Delta\phi \propto f_c \Delta R$. This increases the sensitivity of CW and LFMCW radars.

C. Noise Impact

In radars where the received signal is mixed with a replica of the transmitted signal, such as CW and LFMCW radars, the beat frequency should be kept away from the low-frequency noisy range to guarantee a robust performance. Fig. 3 shows the main noise sources affecting this type of systems: thermal noise, phase noise and flicker noise. However, the low-frequency spectrum is often not clean due to other effects, such as the direct antenna coupling from the TX to the RX. The noise impact is higher in CW radars because two main reasons:

- Noise distribution. CW radars are affected by all the noise sources, as shown in Fig. 3. On the other hand, in LFMCW radars, the beat frequency can be adjusted to separate it from the noise sources that are present around 0 Hz. In fact, it can be placed at higher frequencies where impact of flicker noise is lower than thermal noise.

[1]Mathematically, the slow time can be expressed as $\tau_i = i \cdot T$, with $i \in \mathbb{Z}$, so it is a sampled version of the fast time$t$

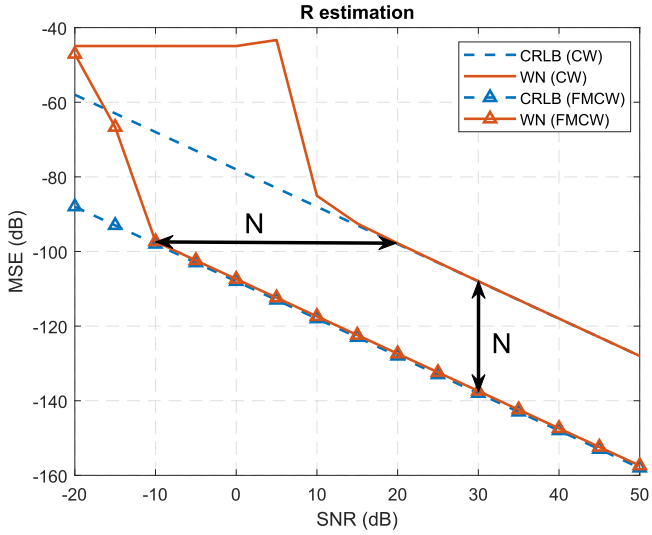

Fig. 4. Displacement estimation with thermal noise for the CW and FMCW configurations. Example with N=1000 samples, which implies an improvement of 30 dB in the R estimation and in the SNR. Simulation: 1000 iterations.

- Processing. The signal estimation is performed in CW radar sample by sample, while in LFMCW configuration is performed in each sweep time by a filterbank of N filters implemented via an N-FFT. Thus, being $N = f_s \cdot T$, where f_s is the sampling frequency and T the sweep time, LFMCW has an estimation improvement of N, as can be shown in (3) and (4), extracted from [34]. This can also be seen in the CramÃ©r-Rao lower bounds (CRLB) presented in Fig. 4.

$$var(\hat{R}) \geq \left(\frac{c}{4\pi f_c}\right)^2 \frac{\sigma^2}{2\,A^2} \tag{3}$$

$$var(\hat{R}) \geq \left(\frac{c}{4\pi}\right)^2 \frac{\sigma^2}{2\,A^2} \frac{1}{N f_c^2 + B f_c (N-1) + \frac{B^2(2N-1)(N-1)}{6N}} \tag{4}$$

where A^2/σ^2 is the signal-to-noise ratio, f_c is the radar working frequency, B is the transmitted bandwidth and N is the signal length.

D. Signal Processing

The algorithm steps to obtain the target displacement in each radar configuration are displayed in Fig. 5.

1) CW: Before using the in-phase and quadrature signals, a calibration process is carried out to compensate the amplitude and phase mismatches and dc-offsets [35]. The analysis of the errors introduced due to imbalances and dc-offsets is detailed in Appendix A. The amplitude and phase imbalances do not change significantly over time, since they are mainly generated by hardware imperfections, so these imbalances can be easily calibrated using compensation methods [36]. However, the dc-offset also comes from reflections from stationary objects around the target [37]. Thus, the correction needs to be run at

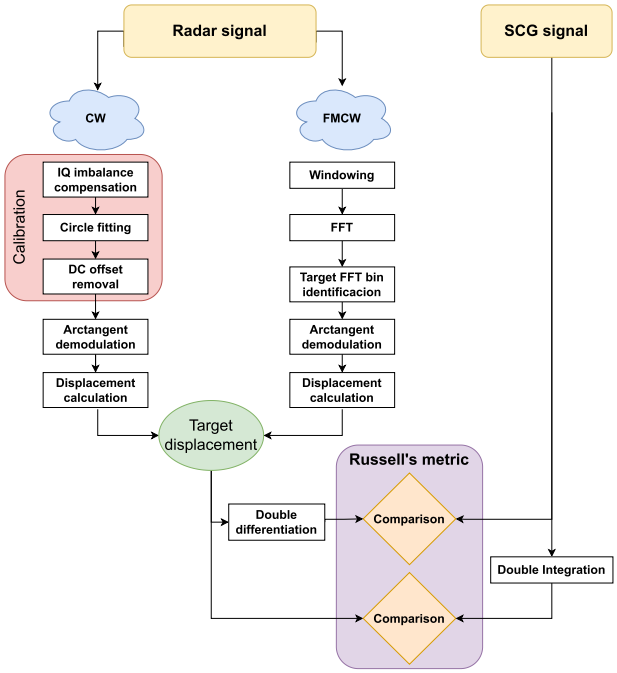

Fig. 5. Flowchart with the processing steps to obtain the target displacement in CW and LFMCW configurations, and its comparison with the SCG signal.

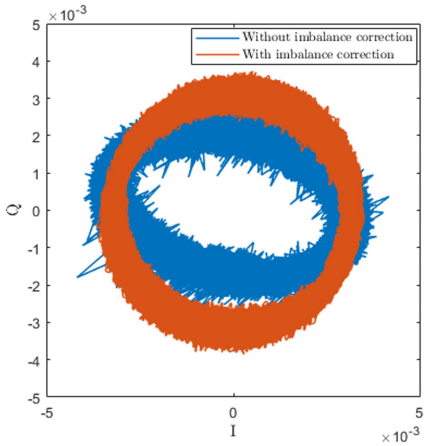

Fig. 6. IQ imbalance correction example. It shows the IQ signals before the calibration -in blue- and after the calibration -in red-.

the beginning of a new measurement each time the environment changes.

The amplitude and phase imbalances provoke that the joint plot of I and Q signals forms an ellipse instead of a circumference. Thus, the ellipse fitting estimation method in [38] is applied. Once the fitting ellipse is defined, the Gram–Schmidt's technique [39] is applied to compensate and correct the imbalances. After that, the Pratt's method [40] is performed to obtain the best-fit circle so as to obtain the circle center, i.e., the dc-offset. The IQ imbalance compensation is shown in Fig. 6. After the dc-offset removal, the arctangent demodulation is carried out to obtain the target's displacement. The calibration process is challenging when the I/Q components do not complete a closed circle, since the estimation of the center of an arc is more prone to errors than the center estimation of a circle, as will be shown in Section IV.

Finally, the arctangent demodulation is performed before calculating the displacement:

$$\Delta R(t) = \frac{unwrap\{\phi(t) - \phi(t_0)\} \cdot c}{4\pi \cdot f_o} \tag{5}$$

where $\phi(t_0)$ is the initial phase at $t = t_0$. Phase must be unwrapped because it takes values between $-\pi$ and π.

A third-order Butterworth low-pass filter with a cut-off frequency of 100 Hz is applied to the I and Q signals before the calibration process.

2) LFMCW: The signal acquired with the radar needs a previous processing to obtain the target displacement. However, unlike the CW processing steps, it does not require a calibration process, as detailed in Appendix A. First of all, a four-term Blackman-Harris window is applied to the in-phase and quadrature signals to enhance the dynamic range. After that, an FFT is performed to identify the frequency range where the target's beat frequency is located. Then, the FFT is clipped in the predefined frequency range, with the aim of isolating the target from interfering objects in the radar's field of view. After that, for each ramp, the phase is computed at the beat frequency, which is calculated as the maximum of the FFT in the frequency range previously calculated.

Finally, the displacement calculation is carried out. Analogously to the CW case, the displacement signal has the following expression:

$$\Delta R(\tau) = \frac{unwrap\{\phi(\tau) - \phi(\tau_0)\} \cdot c}{4\pi \cdot f_c} \tag{6}$$

where $\phi(\tau_0)$ is the initial phase. Nevertheless, the phase extracted has to be corrected to deal with the range migrations because the target can change between range bins of the FFT along the time. We present a new technique that combines the phase and frequency information from the range bin to extract the displacement information. The complete analysis is detailed in Appendix B and the phase, $\phi(t)$, is extracted following (27).

3) SCG: The signal obtained from the SCG does not need a previous conditioning, since it is filtered by hardware in the 0-50 Hz range. In order to perform the comparison with the signal obtained with the radar, this signal is double integrated to obtain the displacement from the acceleration data captured.

E. Comparison Metrics

In order to compare the performance of both configurations, two main comparison have been carried out:

- *Signal waveform:* The displacement measured with the radar is compared with the displacement signal derived from the SCG sensor to quantify which radar configuration reproduces more accurately the waveforms. This comparison is evaluated by using the Russell's error measure [41].
- *Fiducial points:* The radar performance is evaluated by comparing the HRV sequence extracted from the radar with the HRV sequence extracted from the ECG.

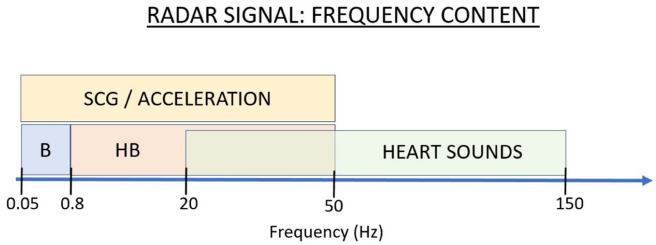

Fig. 7. Frequency range for signal separation: breathing signal (B), heartbeat signal (HB), acceleration signal and heart sounds.

1) Russell's Metric: This metric [41] provides robust means for quantifying the magnitude and phase differences between two time histories separately, and the comprehensive error. For two time series $s1$ and $s2$, with energy E_{s1} and E_{s2}, and length N, the magnitude error is defined as:

$$\sigma_M = sign(rme) log_{10}(1 + |rme|) \tag{7}$$

where *rme* represents the relative magnitude error, which is defined as the following expression:

$$rme = \frac{E_{s_1} - E_{s_2}}{\sqrt{E_{s_1} \cdot E_{s_2}}} \tag{8}$$

The following equation represents the phase error:

$$\sigma_P = \frac{1}{\pi} \cos^{-1} \left(\frac{\sum_{i=1}^{N} s_{1i} \cdot s_{2i}}{\sqrt{E_{s_1} \cdot E_{s_2}}} \right) \tag{9}$$

And the comprehensive error results in the next equation:

$$\sigma_C = \sqrt{\frac{\pi}{4}(\sigma_M^2 + \sigma_P^2)} \tag{10}$$

2) HRV: Unlike heart rate, which focuses on the average beats per minute, the heart rate variability sequence measures the changes in time intervals between adjacent heartbeats. Thus, it is necessary to define the characteristic points for the extraction. The signals and the cardiac events from which the HRV sequence is extracted are explained in more detail in Section III.

III. Vital Signs Monitored With Radar

Different vital signs can be obtained using radar technology. Traditionally, the vital sign parameters retrieved from the radar signal are the respiratory and heart rates. The cardiorespiratory signal has been thoroughly analyzed in the literature, allowing a fair characterization of its components. The heartbeat signal has a fundamental frequency between 0.9 and 3 Hz (54 to 180 beats/min), and an amplitude around 0.5 mm measured from the chest. On the other hand, the breathing signal has a fundamental frequency between 0.1 and 0.7 Hz (6 to 42 breaths/min), and an amplitude between 4 and 12 mm measured from the chest [42]. However, recent studies suggest that information related with specific cardiac events can also be measured analyzing higher frequencies: opening and closure of valves, and heart sounds [13]. Fig. 7 shows how the vital signs are distributed along the frequency range [42], [43]. An example of the displacement signal acquired with the radar is displayed in Fig. 8. Additionally, all the waveforms that can be obtained from the LFMCW and CW radars are displayed in Fig. 9 and 10, respectively, which have been obtained using both radar configurations simultaneously. Therefore, the following information can be extracted from the radar signals:

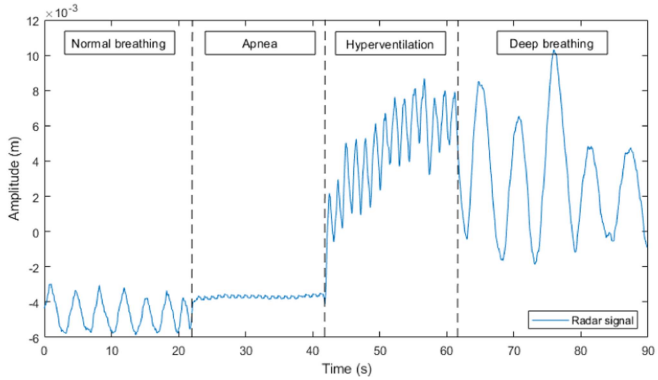

Fig. 8. Displacement signal acquired with the radar setup in LFMCW configuration. From left to right: normal breathing, apnea, hyperventilation and deep breathing time intervals.

1) Breathing and Heart Rates: These rates can be obtained by performing a Fast Fourier Transform (FFT) to the radar displacement signal and looking for the fundamental components [44], [45].

2) Breathing and Heartbeat Waveforms: The breathing and heartbeat signals can be separated, for instance, by linear filtering in the frequency bands shown in Fig. 7. The breathing waveform has practically the same shape that the radar signal, since the breathing amplitude is approximately 10 times higher than the heartbeat signal [42]. Therefore, by inspecting the radar signal, it can be observed anomalies in the respiration, such as, apnea episodes or sudden changes in the breath rate. These phenomena are illustrated in Fig. 8, where an apnea and hyperventilation episodes have been forced and captured with the radar setup, and can be identified at a glance. On the other hand, the heartbeat waveform can be retrieved with band-pass linear filtering. In this work, the heartbeat waveform is defined in the frequency range from 0.8 to 50 Hz, in order to compare it with the data extracted from the SCG. From this signal, some cardiac parameters, such as the HRV sequence, can be calculated. An example of the breathing and heartbeat waveforms extracted with the radar can be shown in Fig. 9(c), (d), 10(c) and (d).

3) Heart Sounds: The pressure waveform resulting from the aperture and closing of the different valves, which is highly correlated with the heart sound waveform obtained with the phonocardiograph [13], can also be obtained from the radar signal. The shape of the heart sound signal obtained from the radar in Fig. 9 e strongly correlates with the heart sound signal measured with the PCG (see Fig. 1 in [46]), which shows the first and second heart sounds (S1 and S2, respectively). The first heart sound occurs directly after the R-peak of the ECG signal, and it is result of the closure of the atrioventricular valves. On the other hand, the second heart sound is a result of the

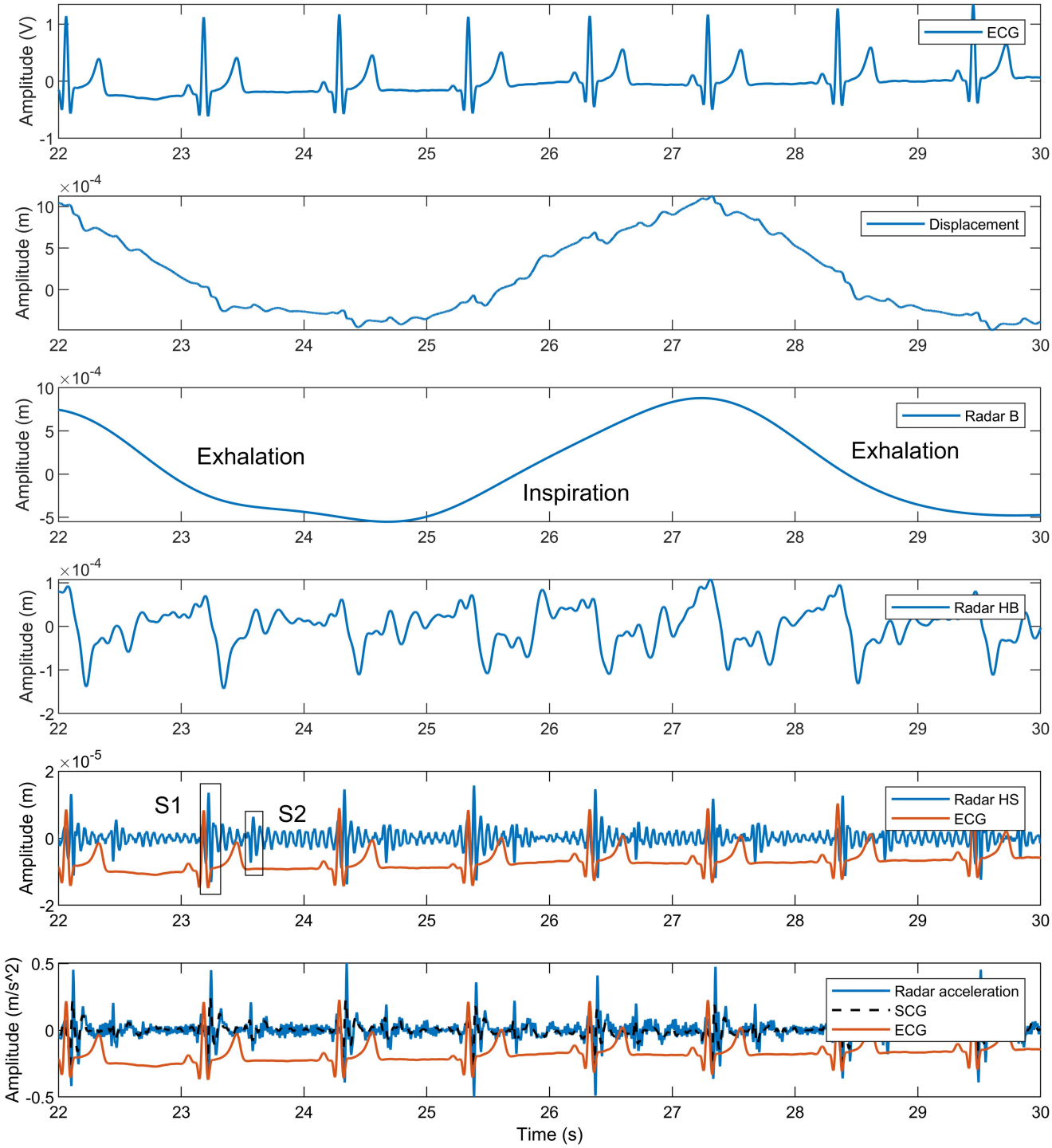

Fig. 9. Comparison between the signals that can be acquired with the LFMCW radar and the reference sensors. From top to bottom: (a) ECG signal, (b) raw radar signal, (c) breathing signal (Radar B), (d) heartbeat signal (Radar HB), (e) heart sound signal (Radar HS), and (f) acceleration signal (Radar acceleration).

sudden closure of the aortic and pulmonary valves. The spectrum of heart sound signals have been analyzed in the literature, and the main information of its components its placed in the 20-150 Hz range [47]. Thus, a linear filtering from 20 to 150 Hz is applied to the radar signal to obtain the heart sound waveform. The amplitude of S1 is higher than S2, so detecting this heart sound is easier than S2. However, it has to be also highlighted that the heart sounds can be modulated due to the breathing. During inspiration, the S1 decreases its intensity, whereas the S2 increases its amplitude [48]. The extraction and identification of the different heart sounds from the radar signal was previously addressed in [13].

4) Acceleration Signal: Some cardiac events can be better identified after a previous preprocessing of the radar signal.

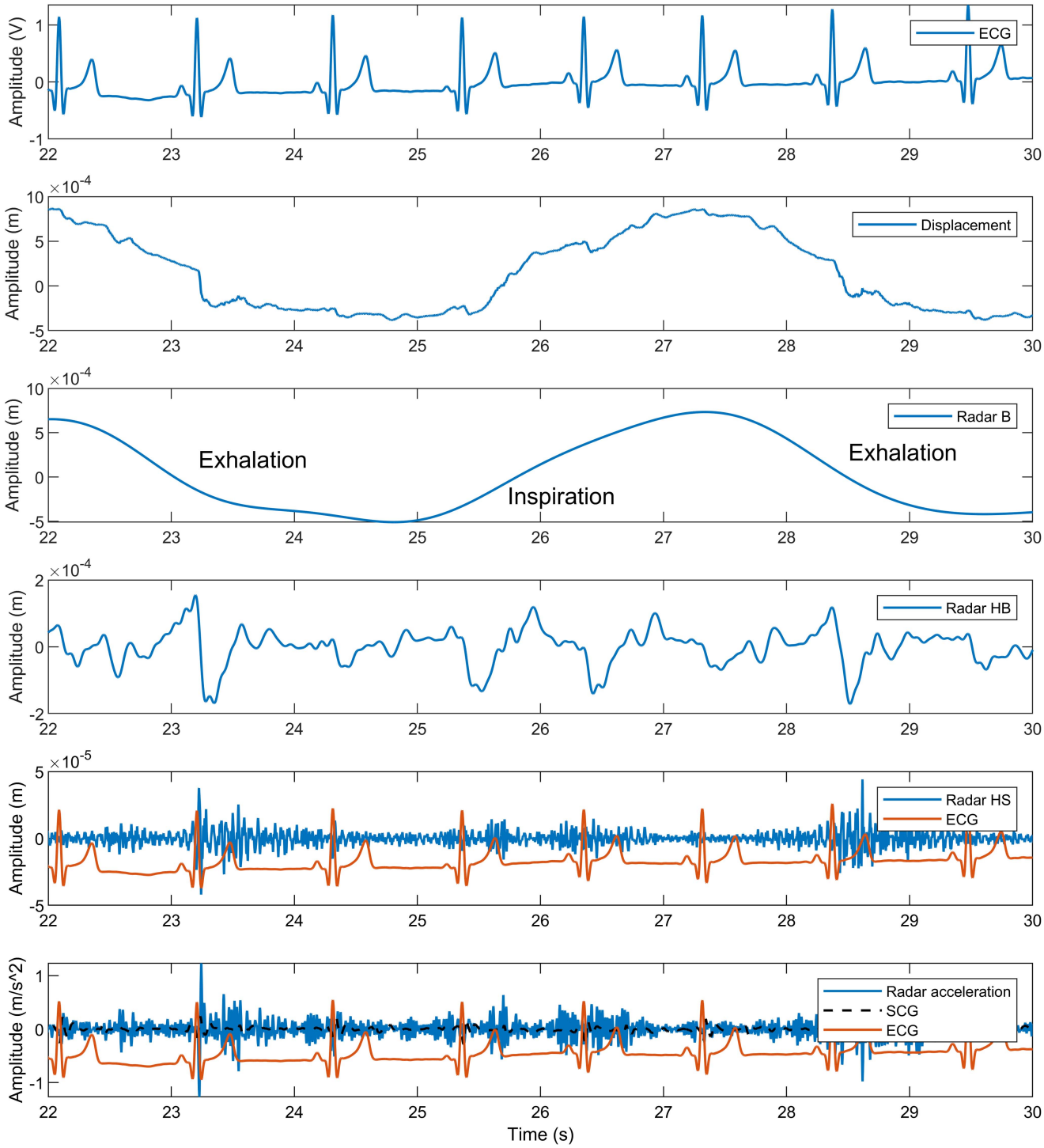

Fig. 10. Comparison between the signals that can be acquired with the CW radar and the reference sensors. From top to bottom: (a) ECG signal, (b) raw radar signal, (c) breathing signal (Radar B), (d) heartbeat signal (Radar HB), (e) heart sound signal (Radar HS), and (f) acceleration signal (Radar acceleration).

Because the radar signal acquired has displacement information of the chest, the double differentiation of this signal provides information on acceleration. This acceleration signal have the same nature as the signal provided by an SCG, therefore, some characteristics events, such as the aortic valve opening (AO), the mitral valve closing (MC), the aortic valve closing (AC), or the mitral valve opening (MO) shown in [46], can be identified. A comparison between the SCG reference and the acceleration signal extracted from the radar is displayed in Fig 11. Moreover, there are studies in the literature that are able to identify these time events. For instance, a deep learning approach is presented in [11] to transform the signal acquired with the radar into an SCG signal, identifying the aforementioned fiducial points. Regarding the frequency content, authors in [43], [49]

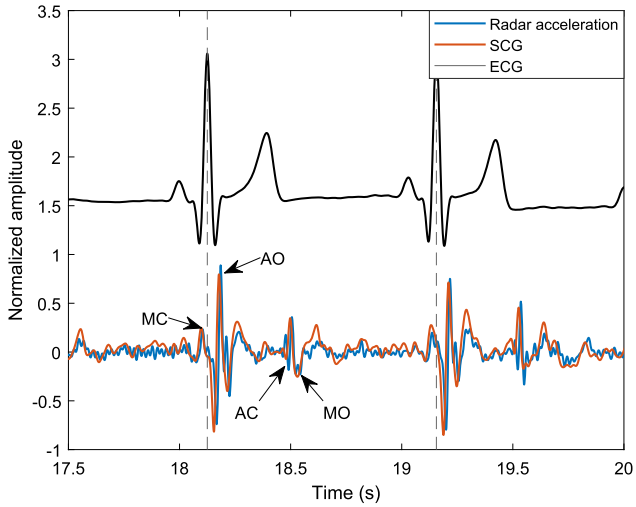

Fig. 11. Comparison between the radar double differentiation and the SCG signal. Locations of ECG R-peaks are marked with dashed lines. The radar signal is acquired using LFMCW configuration.

analyzed the similarities between the SCG signal and the radar acceleration, stating that a high correlation was obtained analyzing the frequency range below 35 Hz. However, [50] shows that there is SCG information above 40 Hz related to valve closure. In this paper the radar acceleration signal is analyzed in the 0-50 Hz frequency range, since the reference SCG used is limited to this band. Figs. 9(f) and 10(f) show the acceleration signal obtained from the radar. From these figures, it can be highlighted that CW radars have difficulties in the extraction of both the acceleration signal and the heart sounds. As was explained in Section II, the impact of the low-frequency noise is higher in CW radars, which can mask these fiducial points in the extracted signals.

5) HRV: This biometric has been calculated measuring the specific changes in time between successive heart beats, as can be shown in Fig. 12(a). These time intervals has been extracted from the different signals following the next procedure:

- The time intervals used to calculate the HRV sequence from the ECG are obtained by measuring the time difference between R-peaks extracted using the Pan and Tompkins algorithm [51].
- The time intervals used to extract the HRV sequence from the heartbeat waveform are calculated by measuring the distance between minima, as displayed in Fig. 12. These minima have been chosen as reference points since they are clearly identifiable for each heart beat. Additionally, the minimum distance between consecutive minima is restricted to be greater than $1/(2f_{hb})$, where f_{hb} is the heartbeat fundamental frequency.
- The post-processing carried out on the acceleration signal calculation improves the cardiac information extraction. Therefore, the HRV sequence can be computed with higher accuracy. The time intervals used to calculate the HRV sequence from the acceleration signal are extracted by measuring the distance between maxima applying the same restriction previously detailed. These maxima do not match the time instants selected in the heartbeat waveform to compute the HRV. As mentioned above, the maxima from the acceleration radar correlate with the aortic opening (AO) that can also be observed in the SCG. This is displayed in Fig. 11.

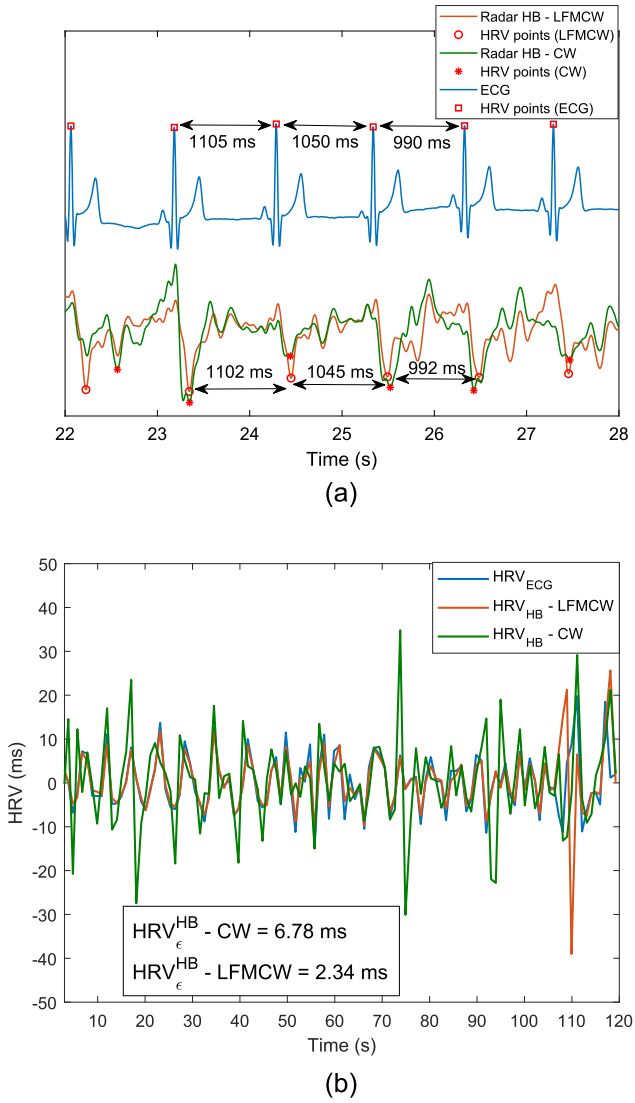

Fig. 12. HRV sequences comparison. (a) Point identification for HRV sequence extraction. (b) The HRV sequence extracted from the heartbeat signal is compared with that one computed from the ECG, with a mean absolute error of 6.78 ms -in CW- and 2.34 ms -in LFMCW-.

The HRV sequence extracted from the heartbeat waveform (displacement signal) is label as HRV_{HB}, while the HRV extracted from the acceleration signal is label as HRV_{Acc}.

Figs. 12 and 13 show that extracting the HRV sequence from the acceleration signal provides better results than using the heartbeat signal. Fig. 12 displays the HRV sequence from the heartbeat waveform for the LFMCW and CW radars. It is important to point out that the waveform shape changes between beats, making the HRV sequence extraction challenging, as is

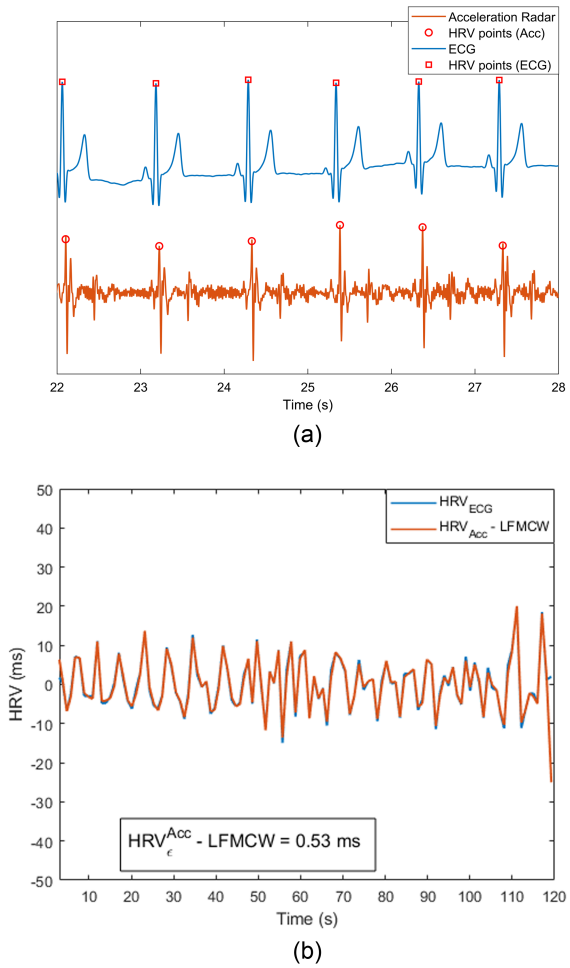

Fig. 13. HRV sequences comparison. (a) Point identification for HRV sequence extraction. (b) The HRV sequence extracted from the acceleration signal is compared with that one computed from the ECG, with a mean absolute error of 0.53 ms.

displayed in Fig. 12(a), where it also shows that there are even differences between the heartbeats waveform obtained with both radars. On the other hand, Fig. 13 shows the HRV sequence from the acceleration radar signal. The time instants (radar AO) are easily identifiable, as is shown in Fig. 13(a), allowing an easier HRV sequence extraction. In this example, the mean absolute error between the HRV sequence extracted from the radar and the ECG is calculated. The error obtained using acceleration is 0.53 ms, while using the heartbeat waveforms the mean error is 2.34 ms using the LFMCW radar, and 6.78 ms in the CW case. Finally, histograms with the error distribution are shown in Fig. 14 for the different strategies to calculate HRV sequence (Fig. 12 and 13). Fig. 14(a) shows that the errors obtained when the HRV sequence is extracted from the heartbeat waveforms are more scattered (larger standard deviation) than when the acceleration signal is used. These results clearly show the improvement of using the radar acceleration instead of the heartbeat waveform in the HRV sequence extraction. This procedure is only possible with the LFMCW radar (see Figs. 9 and 10) because the information is not masked by noise.

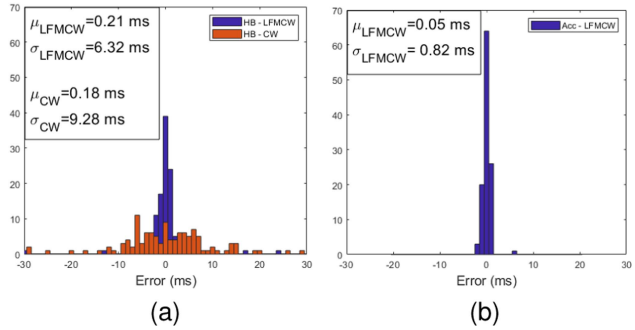

Fig. 14. Histograms with the HRV error distribution for 116 heart beats, and the mean and standard deviation from each distribution. (a) Histograms with the error distribution between the HRV sequence measured with the ECG and the HRV sequence computed from the heartbeat waveform in CW and LFMCW configurations. (b) Histogram with the error distribution between the HRV sequence extracted from the radar acceleration in LFMCW and the ECG.

IV. Comparison Study

This section details the three main experiments carried out in this work. Firstly, a comparison between both radar configurations in a controlled scenario is presented, where the membrane from a woofer is excited with different waveforms to induce controlled displacements of the membrane. Secondly, the vital signs from a person, in a real scenario, are measured. Both radar configurations are used simultaneously, and these signals are compared with the references obtained with the SCG and TFM, which are sampled at 1 kHz. Finally, the vital signs from a person are measured using the 24 GHz MMIC board, in order to confirm the conclusions obtained from the previous experiment carried out at 134 GHz.

For the first two experiments, the LFMCW radar is configured with a sweep time of 1 ms and a bandwidth of 6 GHz. Radar signals are sampled at 10 MHz. The signal processing described in Section II is followed for each configuration. Finally, in order to compare the radar signals with the references obtained from the SCG and the TFM, the displacement signals obtained from the radars are downsampled to the same frequency, 1 kHz, for synchronization.

A. Controlled Scenario

The analysis is carried out by comparing the woofer membrane displacement measured with the SCG and the radar. The radar is placed 0.5 m away from a commercial woofer which is excited with a known waveform, as can be shown in Fig. 15. The field-of-view (FoV) at this distance is a circle of 3.5 cm in diameter. In order to simulate a vital sign monitoring scenario, the woofer is excited with 3 different waveforms to generate the following displacements:

- *Waveform 1:* A sinusoidal displacement of 0.2 Hz and 2 mm of amplitude, which simulates the breathing signal.
- *Waveform 2:* A sinusoidal displacement of 1.1 Hz and 0.2 mm of amplitude, which simulates the heartbeat in apnea condition.
- *Waveform 3:* The sum of the previous 2 signals, which simulates the cardiorespiratory signal.

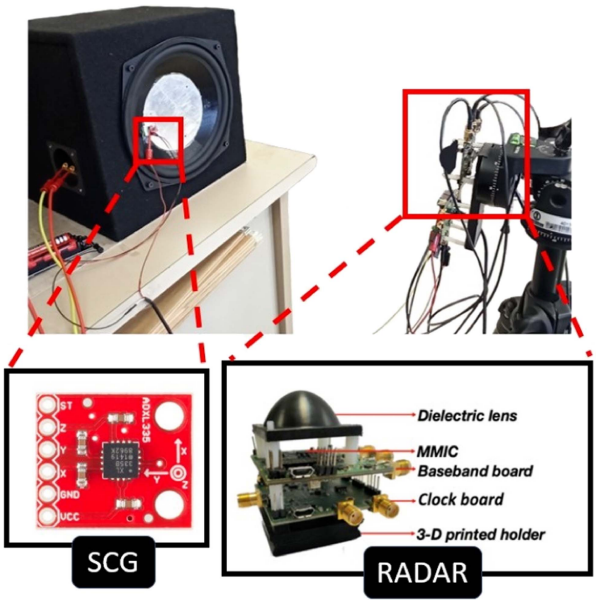

Fig. 15. Controlled scenario: the woofer membrane displacement is measured with an SCG and a radar placed at 0.5 m from the target, simultaneously. The SCG is attached to the woofer membrane.

TABLE II
EXPERIMENT 1: LFMCW VS CW UNDER A CONTROLLED SCENARIO

	LFMCW		CW	
	$\int\int_{SCG}\, dt^2$	$\frac{d^2}{dt^2}_{Rad}$	$\int\int_{SCG}\, dt^2$	$\frac{d^2}{dt^2}_{Rad}$
Waveform 1	0.0375	0.2295	0.0319	0.4910
Waveform 2	0.0623	0.2665	0.4882	1.077
Waveform 3	0.0354	0.1079	0.0324	0.2397
Waveform 3 - HB	0.0723	0.2834	0.0730	0.5742

Russell error obtained for the first approach ($\int\int_{SCG}\, dt^2$) and the second approach ($\frac{d^2}{dt^2}_{Rad}$) for each waveform. *Waveform 3 - HB* is the result of band-pass filtering *Waveform 3* to simulate the heartbeat waveform extraction.

For each waveform, the membrane displacement is captured with the radar operating in CW and LFMCW configurations, and these signals are compared with the SCG used as ground truth. The radar measures displacement information, while the SCG retrieves acceleration information. Both signals are analyzed (displacement and acceleration) since they have useful information, as was previously stated in Section III. Thus, two approaches are employed to compare the radar signals acquired:

- The first approach compares displacement information. Therefore, the SCG signal is double integrated to obtain the displacement information from the acceleration, and the resulting waveform is compared with the radar signal.
- The second approach compares acceleration information. Hence, the radar signal is double differentiated to obtain the acceleration information from the displacement, and this signal is compared with the data from the SCG.

The integration and derivation steps are carried out in the frequency domain with the whole length of the signals. Table II shows the Russell error obtained for the comparison of each waveform.

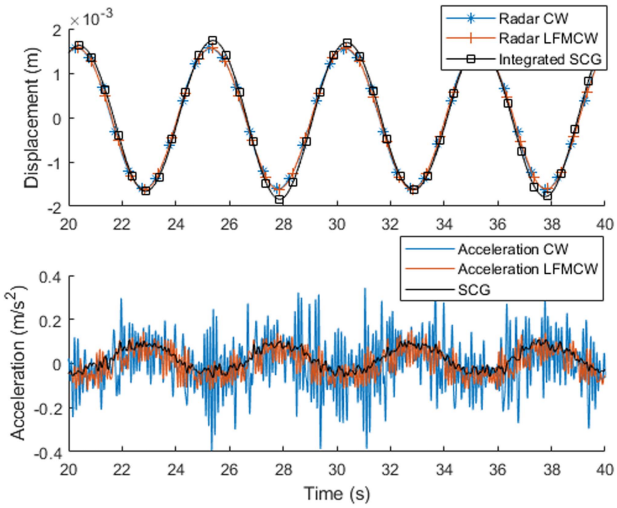

Fig. 16. *Waveform 1* case: Comparison between the radar signal acquired using CW, LFMCW and the reference SCG.

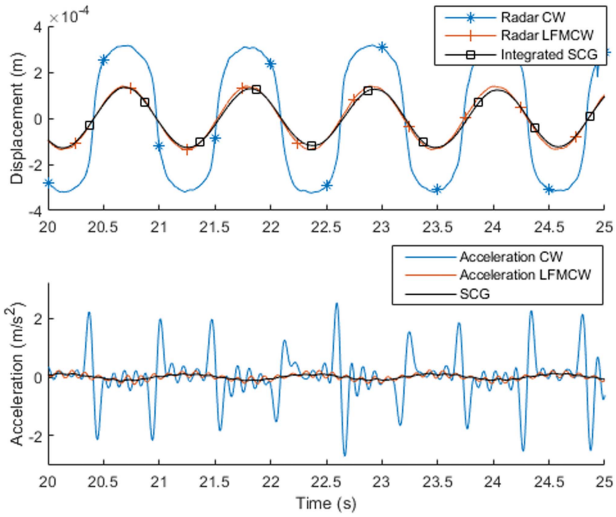

Fig. 17. *Waveform 2* case: Comparison between the radar signal acquired using CW, LFMCW and the reference SCG.

Moreover, the extraction of the heartbeat signals from the cardiorespiratory signal has been also simulated. A band-pass filter is applied from 0.8 to 50 Hz to *Waveform 3* so as to extract the simulated heartbeat waveform. The extracted waveform is compared with the integrated SCG, which has also been filtered using the same filter (it is displayed in Table II as *Waveform 3 - HB*).

The comparison of the different waveforms can be shown in Figs. 16, 17 and 18. These figures show both approaches: top figures represent waveforms for displacement and bottom figures represent acceleration waveforms.

Regarding the comparison carried out with the first approach (displacement analysis), results reflect that both configurations extract accurate results. Table II shows that the differences between both radar configurations are minimum for the *Waveform 1* and *Waveform 3* cases. However, these results show larger

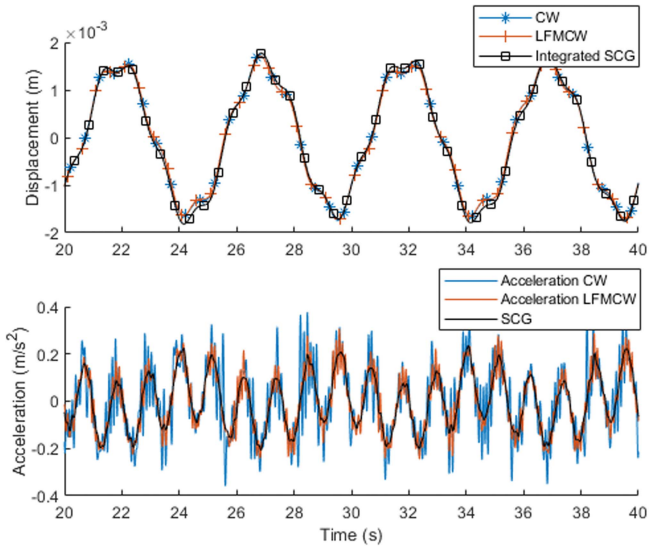

Fig. 18. *Waveform 3* case: Comparison between the radar signal acquired using CW, LFMCW and the reference SCG.

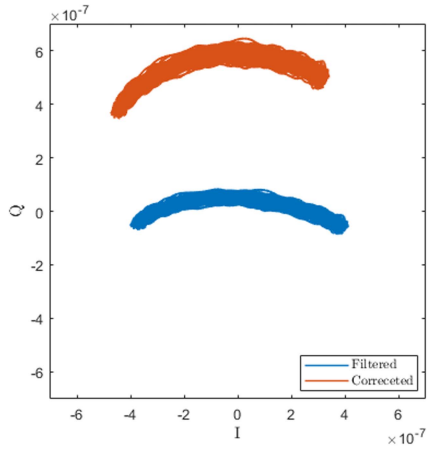

Fig. 19. IQ imbalance correction for *Waveform 2*. It shows the IQ plot after noise filtering -in blue- and after the imbalance calibration -in red-.

differences in *Waveform 2*, this is caused by a non accurate imbalance correction in CW configuration. Although it was stated in [24] that CW was more sensitive to small vibrations, it is also highly dependent on a good calibration. In *Waveform 2* case, the displacement signal to be measured (0.2 mm) is significantly smaller than the wavelength (2.2 mm). At 134 GHz, a vibration movement of 0.2 mm of amplitude covers, approximately, 20% of the I/Q circle, as displayed in Fig. 19. The calibration process is challenging when the I/Q components do not complete a closed circle, and the phase extraction is not accurate, as is displayed in Fig. 17. Since the circle is not complete, the center estimation is not accurate and the dc-offset cannot be removed efficiently. Therefore, the error measured with the radar operating in CW is significantly higher. Notwithstanding, there are studies in the literature that address this issue, for instance, the authors from [36] propose a CW radar with four-phased local oscillator signals to generate multiarcs, which enhances the center estimation but requires a more complex architecture.

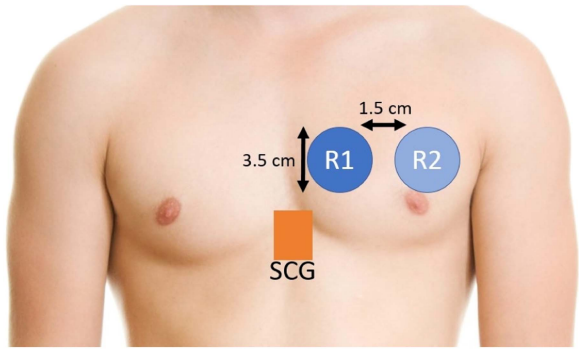

Fig. 20. FoV covered with each radar and SCG placement.

Fig 18 shows the multi-component waveform, whose shapes can be compared with the cardiorespiratory waveform obtained in Figs. 9 and 10. Although this signal contains a small displacement, such as *Waveform 2*, the total displacement in *Waveform 3* allows a proper calibration. It is shown in Table II, where the smaller component is extracted accurately with both radars (*Waveform 3 - HB*).

Regarding the second approach (acceleration analysis), the comparison carried out in Table II between the acceleration signal from the radar and the SCG signal shows that LFMCW radar performs better than CW radar. This fact can be seen at a glance in Figs. 16 and 18: the signals obtained from the CW radar are noisier. The higher noise present in CW, as was explained in Section II, is magnified due to the double differentiation, because it acts as a high pass filter. This means that HRV cannot be accurately extracted using acceleration when the radar is used in CW configuration. This is also analyzed in the vital sign scenario (Tables III and IV).

B. Vital Sign Scenario

The first experiment carried out in this scenario is performed by measuring the vital signs of a person under test (PUT) with the two radars simultaneously: one operates in CW, while the other operates in LFMCW. The PUT is lying down in supine position and the radar setup is pointing with normal incidence to its chest at 0.5 m. Both radars are placed adjacently in order to point to the same chest region. However, due to the narrow beamwidth, the FoV of both radars do not overlap, as displayed in Fig. 20. The FoV at 0.5 m is, approximately, a circle of 3.5 cm in diameter. The radar setup is shown in Fig. 21.

The chest surface curvature causes differences in the radar reflection. In order to remove uncertainties resulting from different incidence, the experiment is divided into two stages:

- *First stage:* the radar pointing to R1 operates in CW, while the radar pointing to R2 operates in LFMCW.
- *Second stage:* the radar pointing to R1 operates in LFMCW, while the radar pointing to R2 operates in CW.

Four different measurements have been analyzed, two from each stage. In these measurements, the PUT is asked to breath normally for 120 seconds. The SCG is placed on the xiphoid process [52]. Moreover, the ECG is measured with the Task Force Monitor.

TABLE III
EXPERIMENT 2: LFMCW VS CW IN A VITAL SIGN SCENARIO AT 0.5 METERS WITH THE 134 GHZ RADAR

	R1					
	Mode	**BR (breaths/min)**	**HR$_{ref}$ (bpm)**	**HR$_{rad}$ (bpm)**	**HRV$_{\epsilon}^{HB}$ (ms)**	**HRV$_{\epsilon}^{Acc}$ (ms)**
Meas. 1	CW	11.0	60.5	60	10.38	17.57
Meas. 2	CW	14.5	56.5	56.2	2.24	7.87
Meas. 3	LFMCW	13.0	57.6	57.6	2.77	0.61
Meas. 4	LFMCW	11.5	58.6	58.6	2.34	0.53
	R2					
	Mode	**BR (breaths/min)**	**HR$_{ref}$ (bpm)**	**HR$_{rad}$ (bpm)**	**HRV$_{\epsilon}^{HB}$ (ms)**	**HRV$_{\epsilon}^{Acc}$ (ms)**
Meas. 1	LFMCW	11.0	60.5	60.6	5.55	0.63
Meas. 2	LFMCW	14.5	56.5	56.5	6.26	0.65
Meas. 3	CW	13.0	57.6	57.1	7.82	14.21
Meas. 4	CW	11.5	58.6	58.6	6.78	16.16

BR: Breathing rate (radar). HR$_{ref}$: Heart rate (ECG). HR$_{rad}$: Heart rate (radar). HRV$_{\epsilon}^{HB}$: Mean absolute error between HRV$_{HB}$ and HRV$_{ECG}$. HRVϵ^{Acc}: Mean absolute error between HRV$_{Acc}$ and HRV$_{ECG}$. The measurements with the same numbering are carried out simultaneously.

TABLE IV
EXPERIMENT 3: 24 GHZ VS 134 GHZ IN A VITAL SIGN SCENARIO

	24 GHz MMIC						
	Dist. (m)	**Mode**	**BR (breaths/min)**	**HR$_{ref}$ (bpm)**	**HR$_{rad}$ (bpm)**	**HRV$_{\epsilon}^{HB}$ (ms)**	**HRV$_{\epsilon}^{Acc}$ (ms)**
Meas. 5	0.3	LFMCW	11.2	63.8	63.8	7.41	1.29
Meas. 6	0.3	CW	12.3	61.5	61.5	17.24	18.48
Meas. 7	0.5	LFMCW	14.5	57.1	57.1	10.32	1.37
Meas. 8	0.5	CW	12.3	61.5	59.3	15.76	17.60
	134 GHz MMIC						
	Dist. (m)	**Mode**	**BR (breaths/min)**	**HR$_{ref}$ (bpm)**	**HR$_{rad}$ (bpm)**	**HRV$_{\epsilon}^{HB}$ (ms)**	**HRV$_{\epsilon}^{Acc}$ (ms)**
Meas. 9	0.5	LFMCW	15.7	53.7	53.7	10.18	1.33
Meas. 10	0.5	CW	12.3	58.2	58.2	15.16	19.8

BR: Breathing rate (radar). HR$_{ref}$: Heart rate (ECG). HR$_{rad}$: Heart rate (radar). HRV$_{\epsilon}^{HB}$: Mean absolute error between HRV$_{HB}$ and HRV$_{ECG}$. HRVϵ^{Acc}: Mean absolute error between HRV$_{Acc}$ and HRV$_{ECG}$.

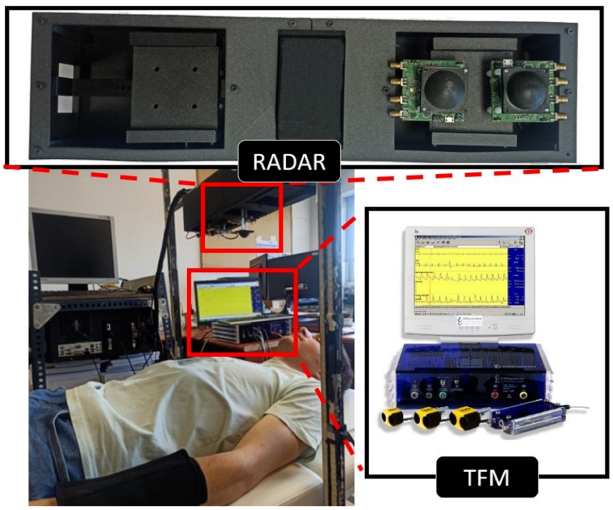

Fig. 21. Vital sign scenario setup. The radar is pointing normally to a subject, who is lying down in supine position at 0.5 m from the radar. The reference signals are acquired with the Task Force Monitor.

In this scenario, the accuracy extracting the different signals detailed in Section III is studied. The breathing rates are compared between radars, while the heart rates are also compared with the reference ECG. The HRV sequence extracted with each radar is compared with the HRV one computed from the ECG. The HRV error is calculated as the mean of the absolute value of the difference between both HRV sequences.

The results are displayed in Table III. It shows, for each measurement:

- The radar configuration (CW or LFMCW).
- The breathing rate (BR).
- The heart rate measured with ECG (HR$_{ref}$) and radar (HR$_{rad}$).
- The mean absolute error between the HRV sequences obtained with the ECG and the HRV sequence extracted with the radar. It is denoted as HRV$_{\epsilon}^{HB}$ if it is extracted from the heartbeat waveform, and as HRV$_{\epsilon}^{Acc}$ if it is computed from the acceleration signal.

Results obtained in the vital sign scenario confirm the conclusions extracted in the previous controlled scenario. Both radar

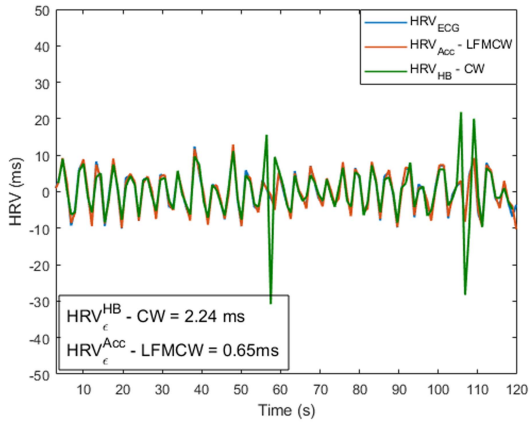

Fig. 22. Comparison between the HRV sequence extracted from the ECG -in blue-, the radar operating in LFMCW -in red-, and the radar operating in CW -in green-. These data belong to *Measurement 2*.

configurations are capable of extracting general metrics, such as breathing and heart rates. The same breathing rate, and almost the same heart rate compared to ECG (reference) are obtained with errors below 1% for both configurations. However, as has been already analyzed, LFMCW has a higher performance in extracting the heart sounds, the acceleration signals and fiducial points from the heartbeat waveform (Figs. 9 and 10). These signals require to analyze higher frequency content from the radar signal, which is more challenging in CW radar since the noise content at higher frequencies tends to mask the signal details. Moreover, the possibility of extracting acceleration information from the radar signal improves the identification of important cardiac events, such as the aortic opening and, therefore, the HRV sequence extraction [53]. Additionally, Figs. 12 and 13 show that extracting the HRV sequence from the acceleration signal provides better results than from the heartbeat waveform. For instance, Fig. 22 shows that even if the best HRV extraction method for each configuration is chosen, LFMCW presents the best extraction results. The data represented in this figure belong to *Measurement 2*.

A second experiment is carried out to confirm the findings at 134 GHz. In this experiment, the vital signs of a target, which is lying down in supine position in front of the radar, are measured with the 24 GHz radar. However, as was detailed in Section II, the antenna beamwidth of this MMIC board is broader than the one at 134 GHz, so the FoV covered is larger. With the aim of covering a body chest area similar to the previous experiment, the PUT is measured at 0.3 and 0.5 meters. The FoV at these distances is 15.5 x 8.4 cm and 25.9 x 14 cm at 0.3 and 0.5 meters, respectively, so it covers R1 and R2 regions simultaneously. Focusing is an important matter in this analysis because some studies show how the heart wave shape changes depending on the area measured [16]. However, the area covered with the 24 GHz MMIC at these distances is still comparable with the heart size (12 x 8 cm [54]). Thus, the HRV can still be extracted accurately.

On the other hand, the parameters used to configure the 24 GHz LFMCW radar are different from the previous experiment, due to the bandwidth at 24 GHz is limited to 3.6 GHz. With the aim of having a beat frequency comparable with *Experiment 2* ($f_b \simeq 20$ kHz), the radar has been configured to transmit a bandwith of 2 GHz and the sweep time has been set to 200 μs. Therefore, so as to compare these results with those obtained in Table III, the PUT has also been measured with the 134 GHz radar using the same configuration parameters. The measurements carried out at 134 GHz have been performed pointing at R1.

Results are presented in Table IV, which follows the same structure than Table III. Results obtained with the 24 GHz MMIC board prove that the conclusions reached previously do not depend on the radar working frequency:

- LFMCW configuration is better to extract the HRV.
- Results do not depend on the distance, while the FoV is still comparable with the heart size.

On the other hand, measurements at 0.5 meters with the 134 GHz MMIC board show that the results do not depend on the sweep time selected or the transmitted bandwidth, since they are comparable to those presented in Table III (errors of the same order of magnitude).

Therefore, despite both radar configurations are capable of extracting and measuring vital signs with high performance, the use of LFMCW radar over CW is recommended. Using the same hardware architecture, LFMCW configuration allows the extraction of more cardiac information and with higher accuracy.

Moreover, LFMCW configuration allows to measure not only the vital signs of one subject, but also monitor several subjects simultaneously, allowing its tracking and providing location information. These characteristics are basic for rescue-working and tele-health scenarios [55], [56].

V. Conclusion

Radar devices are an appealing solution for noncontact monitoring of vital signs. The comprehensive comparison carried out in this paper between continuous-wave (CW) and frequency-modulated continuous-wave (LFMCW) radar configurations reflects that, although both radars can extract general metrics, such as breathing and heart rates, detailed information can only be extracted in LFMCW radars. It is explained that CW radar performance is more affected by low frequency noise, making challenging or unfeasible the extraction of heart sounds or the desired fiducial points from the acceleration signal. Moreover, this causes that the HRV sequence extraction is more accurate in LFMCW radars, since it can be computed from the acceleration signal. It has also be highlighted that CW radars, unlike LFMCW radars, are highly dependent on calibration. Besides, LFMCW configuration allows multi-target monitoring simultaneously, which is essential in assisting living monitoring environments.

Appendix A
IQ Imbalance Influence in Phase Extraction

A. CW

The phase extraction in CW radars is carried out by performing the arctangent demodulation of the beat signal. The beat

signal defined in (1) can also be expressed as:

$$s_b(t) = I(t) + jQ(t) \tag{11}$$

where $I(t)$ and $Q(t)$ are the in-phase and quadrature signal components, respectively. Nonideal systems induce amplitude and phase imbalances between both channels which have to be calibrated. Additionally, there are dc-offset problems that have to be addressed in the I/Q demodulation. Therefore, the I- and Q-channels have the following expressions:

$$\begin{aligned} I(t) &= A_I \cos\left(\frac{4\pi f_c}{c}R(t) + \phi_I\right) + DC_I \\ &= A_I \cos(\Theta_I(t)) + DC_I \end{aligned} \tag{12}$$

$$Q(t) = A_Q \sin\left(\frac{4\pi f_c}{c}R(t) + \phi_Q\right) + DC_Q \tag{13}$$

where A_I and A_Q are the component amplitude, ϕ_I and ϕ_Q are the initial phase-shift, and DC_I and DC_Q are the signal bias. It is also possible to redefine $Q(t)$ in terms of the amplitude imbalance, $A_\epsilon = A_Q/A_I$, and the phase imbalance, $\phi_\epsilon = \phi_Q - \phi_I$, the resulting expressions are [35]:

$$I(t) = A_I \cos(\Theta_I(t)) + DC_I \tag{14}$$

$$Q(t) = A_I A_\epsilon \sin(\Theta_I(t) + \phi_\epsilon) + DC_Q \tag{15}$$

Therefore, the phase extracted from the beat signal has the following expression:

$$\phi_{meas}(t) = arg(s_b(t)) = \tan^{-1}\left(\frac{Q(t)}{I(t)}\right) = \tan^{-1}\left[\frac{A_\epsilon[\sin(\Theta_I(t))\cos(\phi_\epsilon) + \cos(\Theta_I(t))\sin(\phi_\epsilon)] + \frac{DC_Q}{A_I}}{\cos(\Theta_I(t)) + \frac{DC_I}{A_I}}\right] \tag{16}$$

This result implies that all the channel imbalances and dc-offset affect the phase extraction and have to be previously calibrated.

B. LFMCW

The phase extraction in LFMCW radars is carried out by performing the arctangent demodulation of the beat signal, but unlike in CW systems, it is done in the frequency domain. $I(t,\tau)$ and $Q(t,\tau)$ are the phase and quadrature signal components, respectively. Taking into account the nonideal components aforementioned in the CW case, the I- and Q-channels have the following expressions:

$$I(t,\tau) = A_I \cos\left(2\pi f_b(\tau)t + \frac{4\pi f_c}{c}R(\tau) + \phi_I\right) + DC_I \tag{17}$$

$$Q(t,\tau) = A_Q \sin\left(2\pi f_b(\tau)t + \frac{4\pi f_c}{c}R(\tau) + \phi_Q\right) + DC_Q \tag{18}$$

The beat signal is windowed to enhance the dynamic range and to reduce the interference of unwanted components. Being $w(t)$ the window response, the beat signal can be written as

$$s_b(t,\tau) = (I(t,\tau) + jQ(t,\tau)) \cdot w(t) \tag{19}$$

Performing the Fourier Transform of the beat signal, it follows the next expression:

$$\begin{aligned} S_b(f,\tau) = \frac{A_I}{2}&\left[\delta(f - f_b)\exp\left(j\left(\frac{4\pi f_c}{c}R(\tau) + \phi_I\right)\right)\right. \\ &\left. + \delta(f + f_b)\exp\left(-j\left(\frac{4\pi f_c}{c}R(\tau) + \phi_I\right)\right)\right] * W(f) \\ &+ DC_I\delta(f) * W(f) \\ &+ \frac{A_Q}{2}\left[\delta(f - f_b)\exp\left(j\left(\frac{4\pi f_c}{c}R(\tau) + \phi_Q\right)\right)\right. \\ &\left. - \delta(f + f_b)\exp\left(-j\left(\frac{4\pi f_c}{c}R(\tau) + \phi_Q\right)\right)\right] * W(f) \\ &+ jDC_Q\delta(f) * W(f) \end{aligned} \tag{20}$$

Analyzing (20) at $f = f_b$, it is obtained that:

$$\begin{aligned} &S_b(f_b,\tau) \\ &= \frac{A_I}{2}[1 + A_\epsilon\exp(j\phi_\epsilon)]\exp\left(j\left(\frac{4\pi f_c}{c}R(\tau) + \phi_I\right)\right)W(0) \\ &\quad + \frac{A_I}{2}[1 - A_\epsilon\exp(j\phi_\epsilon)]\exp\left(j\left(\frac{4\pi f_c}{c}R(\tau) + \phi_I\right)\right) \\ &\quad \times W(2f_b) + [DC_I + jDC_Q]W(f_b) \end{aligned} \tag{21}$$

Therefore, since the selected window has side lobe levels higher than 30 dB, the phase extracted can be approximated as

$$arg(S_b(f_b,\tau)) \simeq \frac{4\pi f_c}{c}R(\tau) + \tan^{-1}\left(\frac{A_\epsilon\sin(\phi_\epsilon)}{1 + A_\epsilon\cos(\phi_\epsilon)}\right) \tag{22}$$

where it can be observed that the imbalance due to dc-offset does not significantly modify the extracted phase. On the other hand, if the phase and amplitude imbalances do not vary with time, they can also be ignored, since they are constant. In summary, from (16) and (22), it can be concluded that dc-offset only affects in the phase extraction in CW radars. Additionally, amplitude and phase imbalances have a higher impact in CW configurations.

Appendix B
Phase Correction: LFMCW Case

The beat signal, already defined in (2), follows this expression:

$$s_b(t,\tau) = \exp j(2\pi f_b(\tau)t + \phi(\tau)) \tag{23}$$

where $\phi(\tau) = \frac{4\pi f_c R(\tau)}{c}$. Performing an L-point FFT of the beat signal ($s_b(t,\tau)$), the phase measured evaluating a single bin can be expressed as:

$$\phi_{meas}(\tau) = \phi(\tau) + \phi_{error} \tag{24}$$

where ϕ_{error} represents the phase error since the frequency of the signal $s_b(t)$ does not match with FFT bin. The insertion phase of the filter bank implemented via an L-point FFT is linear from $\frac{-\pi}{2}$ to $\frac{+\pi}{2}$, as is displayed in Fig. 23, so this insertion phase can be model as:

$$\phi_{error} = \frac{\pi}{\Delta f}(f_b - f_{bin}) \tag{25}$$

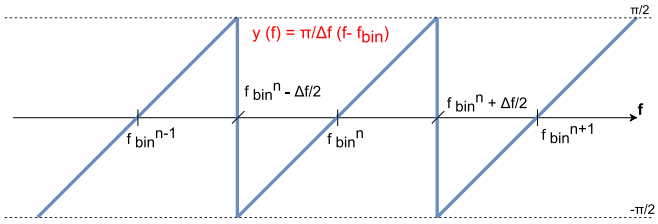

Fig. 23. Insertion phase for the filter bank developed with an FFT.

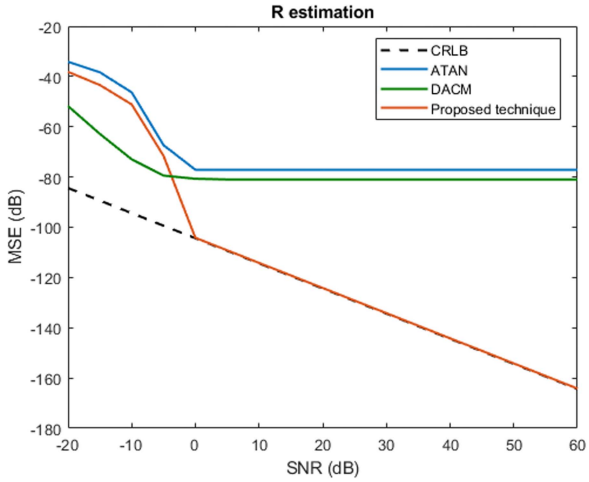

Fig. 24. Range estimation simulation results. The proposed technique (in orange) is compared with the arctangent demodulation (in blue), and the DACM algorithm (in green).

where $\Delta f = f_s/L$ is the bin separation in an L-point FFT, and f_s represents the sampling frequency.

Thus, after performing the L-point FFT, ϕ_{meas} can be model as:

$$\begin{aligned}\phi_{meas}(\tau) &= \frac{4\pi f_c R(\tau)}{c} + \frac{\pi}{\Delta f}(f_b(\tau) - f_{bin}(\tau)) \\ &= \frac{4\pi f_c R(\tau)}{c} + \frac{\pi L}{f_s}(\frac{2BR(\tau)}{Tc} - f_{bin}(\tau)) \\ &= \frac{4\pi f_c R(\tau)}{c} + \frac{2\pi BLR(\tau)}{f_s Tc} - \frac{\pi L f_{bin}(\tau)}{f_s} \end{aligned} \quad (26)$$

Thus, the chest displacement can be expressed by the following equation:

$$R(\tau) = \frac{\phi_{meas}(\tau) + \frac{\pi \mathrm{Lf_{bin}}(\tau)}{\mathrm{f_s}}}{\frac{4\pi f_c}{c} + \frac{2\pi BL}{f_s Tc}} \quad (27)$$

It is also important to highlight that the measured phase from the FFT is wrapped in the $[-\pi, +\pi]$ range, so an unwrapping algorithm has to be applied.

Moreover, the Cramér-Rao lower bound (CRLB) has been calculated. The new approach proposed is compared with the most used methods in the literature to extract the range information from the phase: arctangent demodulation (ATAN) and the differentiate and cross multiply (DACM) algorithm. Results are displayed in Fig. 24, showing that our algorithm reaches the Cramér-Rao bound.

Acknowledgment

The authors would like also to thank Mercé V. Electromedicina [57] for providing the Task Force Monitor to perform the measurements.

References

[1] C. Hülsmeyer, "Verfahren, um entfernte metallische gegenstände mittels elektrischer wellen einem beobachter zu melden," German Patent DE165546C, Apr. 30, 1904.
[2] H. H. Meinel, "Millimeter-wave technology advances since 1985 and future trends," *IEEE Trans. Microw. Theory Techn.*, vol. 39, no. 5, pp. 759–767, May 1991.
[3] W. A. Ahmad and X. Yi, "How will radar be integrated into daily life?: mm-Wave radar architectures for modern daily life applications," *IEEE Microw. Mag.*, vol. 23, no. 5, pp. 30–43, May 2022.
[4] M. I. Hussain, S. Azam, M. A. Rafique, A. M. Sheri, and M. Jeon, "Drivable region estimation for self-driving vehicles using radar," *IEEE Trans. Veh. Technol.*, vol. 71, no. 6, pp. 5971–5982, Jun. 2022.
[5] S. S. Ahmed, "Microwave imaging in security–Two decades of innovation," *IEEE J. Microw.*, vol. 1, no. 1, pp. 191–201, Jan. 2021.
[6] M. Bonmann et al., "Sub-millimetre wave range-Doppler radar as a diagnostic tool for gas-solids systems-solids concentration measurements," *Adv. Powder Technol.*, vol. 34, no. 1, 2023, Art. no. 103894.
[7] H. Zhao, G. Chen, H. Hong, and X. Zhu, "Remote structural health monitoring for industrial wind turbines using short-range Doppler radar," *IEEE Trans. Instrum. Meas.*, vol. 70, pp. 1–9, 2021.
[8] A. T. Purnomo, K. S. Komariah, D.-B. Lin, W. F. Hendria, B.-K. Sin, and N. Ahmadi, "Non-contact supervision of COVID-19 breathing behaviour with FMCW radar and stacked ensemble learning model in real-time," *IEEE Trans. Biomed. Circuits Syst.*, vol. 16, no. 4, pp. 664–678, Aug. 2022.
[9] J. Liu, Y. Li, C. Li, C. Gu, and J.-F. Mao, "Accurate measurement of human vital signs with linear FMCW radars under proximity stationary clutters," *IEEE Trans. Biomed. Circuits Syst.*, vol. 15, no. 6, pp. 1393–1404, Dec. 2021.
[10] J. E. Kiriazi, S. M. M. Islam, O. Borić-Lubecke, and V. M. Lubecke, "Sleep posture recognition with a dual-frequency cardiopulmonary Doppler radar," *IEEE Access*, vol. 9, pp. 36181–36194, 2021.
[11] U. Ha, S. Assana, and F. Adib, "Contactless seismocardiography via deep learning radars," in *Proc. 26th Annu. Int. Conf. Mobile Comput. Netw.*, 2020, pp. 1–14.
[12] D. Buxi, R. Dugar, J.-M. Redouté, and M. R. Yuce, "Comparison of the impedance cardiogram with continuous wave radar using body-contact antennas," in *Proc. IEEE 39th Annu. Int. Conf. Eng. Med. Biol. Soc.*, 2017, pp. 693–696.
[13] C. Will et al., "Radar-based heart sound detection," *Sci. Rep.*, vol. 8, no. 1, pp. 1–14, 2018.
[14] F. Shaffer, R. McCraty, and C. L. Zerr, "A healthy heart is not a metronome: An integrative review of the heart's anatomy and heart rate variability," *Front. Psychol.*, vol. 5, 2014, Art. no. 1040.
[15] O. B. Lubecke, P.-W. Ong, and V. M. Lubecke, "10 GHz Doppler radar sensing of respiration and heart movement," in *Proc. IEEE 28th Annu. Northeast Bioeng. Conf.*, 2002, pp. 55–56.
[16] C. Will et al., "Local pulse wave detection using continuous wave radar systems," *IEEE J. Electromagn., RF, Microw. Med. Biol.*, vol. 1, no. 2, pp. 81–89, Dec. 2017.
[17] G. Wang, J.-M. Munoz-Ferreras, C. Gu, C. Li, and R. Gomez-Garcia, "Application of linear-frequency-modulated continuous-wave (LFMCW) radars for tracking of vital signs," *IEEE Trans. Microw. Theory Techn.*, vol. 62, no. 6, pp. 1387–1399, Jun. 2014.
[18] A. Ahmad, J. C. Roh, D. Wang, and A. Dubey, "Vital signs monitoring of multiple people using a FMCW millimeter-wave sensor," in *Proc. IEEE Radar Conf.*, 2018, pp. 1450–1455.
[19] L. Ren, H. Wang, K. Naishadham, O. Kilic, and A. E. Fathy, "Phase-based methods for heart rate detection using UWB impulse Doppler radar," *IEEE Trans. Microw. Theory Techn.*, vol. 64, no. 10, pp. 3319–3331, Oct. 2016.
[20] C. Gu, "Short-range noncontact sensors for healthcare and other emerging applications: A review," *Sensors*, vol. 16, no. 8, 2016, Art. no. 1169.

[21] C. Li, V. M. Lubecke, O. Boric-Lubecke, and J. Lin, "A review on recent advances in Doppler radar sensors for noncontact healthcare monitoring," *IEEE Trans. Microw. Theory Techn.*, vol. 61, no. 5, pp. 2046–2060, May 2013.
[22] M. Kebe, R. Gadhafi, B. Mohammad, M. Sanduleanu, H. Saleh, and M. Al-Qutayri, "Human vital signs detection methods and potential using radars: A. review," *Sensors*, vol. 20, no. 5, 2020, Art. no. 1454.
[23] S. M. M. Islam, O. Boric-Lubecke, V. M. Lubecke, A.-K. Moadi, and A. E. Fathy, "Contactless radar-based sensors: Recent advances in vital-signs monitoring of multiple subjects," *IEEE Microw. Mag.*, vol. 23, no. 7, pp. 47–60, Jul. 2022.
[24] J.-M. Muíoz-Ferreras, Z. Peng, R. Gómez-García, and C. Li, "Review on advanced short-range multimode continuous-wave radar architectures for healthcare applications," *IEEE J. Electromagn., RF, Microw. Med. Biol.*, vol. 1, no. 1, pp. 14–25, Jun. 2017.
[25] L. Lu, C. Li, and J. A. Rice, "A software-defined multifunctional radar sensor for linear and reciprocal displacement measurement," in *Proc. IEEE Topical Conf. Wireless Sensors Sensor Netw.*, 2011, pp. 17–20.
[26] N. Chahat, M. Zhadobov, R. Augustine, and R. Sauleau, "Human skin permittivity models for millimetre-wave range," *Electron. Lett.*, vol. 47, no. 7, pp. 427–428, 2011.
[27] "Non-invasive, continuous blood pressure and hemodynamic measurement," Jan. 2023. [Online]. Available: https://www.cnsystems.com/
[28] "Radar evaluation kits for various front ends," May 2022. [Online]. Available: https://siliconradar.com/evalkits/
[29] F. A. García Rial, "Technological contributions to imaging radars in the millimeter-wave band," Ph.D. dissertation, ETSIT-UPM, 2019.
[30] "ADXL335 Datasheet," Jan. 2023. [Online]. Available: https://www.analog.com/media/en/technical-documentation/data-sheets/adxl335.pdf
[31] S. Schellenbergeret al., "A dataset of clinically recorded radar vital signs with synchronised reference sensor signals," *Sci. Data*, vol. 7, no. 1, pp. 1–11, 2020.
[32] W. G. Carrara, R. S. Goodman, and R. M. Majewski, "Soptlight synthetic aperture radar," *Signal Process. Algorithms*, Boston, MA, USA: Artech House, 1995.
[33] M. He, Y. Nian, and Y. Gong, "Novel signal processing method for vital sign monitoring using FMCW radar," *Biomed. Signal Process. Control*, vol. 33, pp. 335–345, 2017.
[34] S. M. Kay, *Fundamentals of Statistical Signal Processing: Estimation Theory*. Hoboken, NJ, USA: Prentice-Hall,1993.
[35] W. Hu, Z. Zhao, Y. Wang, H. Zhang, and F. Lin, "Noncontact accurate measurement of cardiopulmonary activity using a compact quadrature Doppler radar sensor," *IEEE Trans. Biomed. Eng.*, vol. 61, no. 3, pp. 725–735, Mar. 2014.
[36] J.-H. Park and J.-R. Yang, "Multiphase continuous-wave Doppler radar with multiarc circle fitting algorithm for small periodic displacement measurement," *IEEE Trans. Microw. Theory Techn.*, vol. 69, no. 11, pp. 5135–5144, Nov. 2021.
[37] B.-K. Park, O. Boric-Lubecke, and V. M. Lubecke, "Arctangent demodulation with DC offset compensation in quadrature Doppler radar receiver systems," *IEEE Trans. Microw. Theory Techn.*, vol. 55, no. 5, pp. 1073–1079, May 2007.
[38] A. Singh et al., "Data-based quadrature imbalance compensation for a CW Doppler radar system," *IEEE Trans. Microw. Theory Techn.*, vol. 61, no. 4, pp. 1718–1724, Apr. 2013.
[39] F. E. Churchill, G. W. Ogar, and B. J. Thompson, "The correction of I and Q errors in a coherent processor," *IEEE Trans. Aerosp. Electron. Syst.*, vol. AES-17, no. 1, pp. 131–137, Jan. 1981.
[40] V. Pratt, "Direct least-squares fitting of algebraic surfaces," *ACM SIGGRAPH Comput. Graph.*, vol. 21, no. 4, pp. 145–152, 1987.
[41] D. M. Russell, "Error measures for comparing transient data: Part I: Development of a comprehensive error measure," in *Proc. 68th Shock Vib. Symp.*, 1997, pp. 175–184.
[42] O. Boric-Lubecke, V. M. Lubecke, A. D. Droitcour, B.-K. Park, and A. Singh, *Doppler Radar Physiological Sensing*. Hoboken, NJ, USA: Wiley, 2015.
[43] Z. Xia, M. M. H. Shandhi, O. T. Inan, and Y. Zhang, "Non-contact sensing of seismocardiogram signals using microwave Doppler radar," *IEEE Sensors J.*, vol. 18, no. 14, pp. 5956–5964, Jul. 2018.
[44] D. T. Petkie, C. Benton, and E. Bryan, "Millimeter wave radar for remote measurement of vital signs," in *Proc. IEEE Radar Conf.*, 2009, pp. 1–3.
[45] Y. Wang, Q. Liu, and A. E. Fathy, "CW and pulse–Doppler radar processing based on FPGA for human sensing applications," *IEEE Trans. Geosci. Remote Sens.*, vol. 51, no. 5, pp. 3097–3107, May 2013.
[46] P. Dehkordiet al., "Comparison of different methods for estimating cardiac timings: A comprehensive multimodal echocardiography investigation," *Front. Physiol.*, vol. 10, 2019, Art. no. 1057.
[47] P. Arnott, G. Pfeiffer, and M. Tavel, "Spectral analysis of heart sounds: Relationships between some physical characteristics and frequency spectra of first and second heart sounds in normals and hypertensives," *J. Biomed. Eng.*, vol. 6, no. 2, pp. 121–128, 1984.
[48] G. Amit, K. Shukha, N. Gavriely, and N. Intrator, "Respiratory modulation of heart sound morphology," *Amer. J. Physiol.-Heart Circulatory Physiol.*, vol. 296, no. 3, pp. H796–H805, 2009.
[49] S. J. Mazlouman, K. Tavakolin, A. Mahanfar, and B. Kaminska, "Contactless assessment of in-vivo body signals using microwave Doppler radar," *Biomed. Eng.*, vol. 13, pp. 239–260, 2009.
[50] A. Taebi and H. A. Mansy, "Time-frequency distribution of seismocardiographic signals: A comparative study," *Bioengineering*, vol. 4, no. 2, 2017, Art. no. 32.
[51] J. Pan and W. J. Tompkins, "A real-time QRS detection algorithm," *IEEE Trans. Biomed. Eng.*, vol. BME-32, no. 3, pp. 230–236, Mar. 1985.
[52] A. Taebi, B. E. Solar, A. J. Bomar, R. H. Sandler, and H. A. Mansy, "Recent advances in seismocardiography," *Vibration*, vol. 2, no. 1, pp. 64–86, 2019.
[53] M. J. Tadi, E. Lehtonen, T. Koivisto, M. Pänkäälä, A. Paasio, and M. Teräs, "Seismocardiography: Toward heart rate variability (HRV) estimation," in *Proc. IEEE Int. Symp. Med. Meas. Appl.*, 2015, pp. 261–266.
[54] S. Mohammadi, A. Hedjazi, M. Sajjadian, N. Ghoroubi, M. Mohammadi, and S. Erfani, "Study of the normal heart size in northwest part of Iranian population: A cadaveric study," *J. Cardiovasc. Thoracic Res.*, vol. 8, no. 3, 2016, Art. no. 119.
[55] S. Z. Gurbuz and M. G. Amin, "Radar-based human-motion recognition with deep learning: Promising applications for indoor monitoring," *IEEE Signal Process. Mag.*, vol. 36, no. 4, pp. 16–28, Jul. 2019.
[56] J. Le Kernec et al., "Radar signal processing for sensing in assisted living: The challenges associated with real-time implementation of emerging algorithms," *IEEE Signal Process. Mag.*, vol. 36, no. 4, pp. 29–41, Jul. 2019.
[57] "Mercé V. Electromedicina," Jan. 2023. [Online]. Available: https://mercev.com/

Elías Antolinos (Student Member, IEEE) was born in Los Martínez del Puerto (Murcia), Spain, in 1995. He received the B.Sc. degree in telecommunications engineering from the Universidad Politécnica de Cartagena, Cartagena, Spain, in 2017, and the Master's degree in telecommunications engineering from the Universidad Politécnica de Madrid (UPM), Madrid, Spain, in 2019. He is currently working toward the Ph. D. degree Microwave and Radar Group, Department of Signals, Systems and Radiocommunications, Universidad Politécnica de Madrid. Since 2018, he has been with the Microwave and Radar Group, Department of Signals, Systems and Radiocommunications, Universidad Politécnica de Madrid. His research interests include radar signal processing, vital sign monitoring, and millimeter-wave radars.

Jesús Grajal (Senior Member, IEEE) was born in Toral de los Guzmanes (León), Spain, in 1967. He received the Ingeniero de Telecomunicacián degree and the Ph.D. degree from the Universidad Politécnica de Madrid, Madrid, Spain, in 1992 and 1998, respectively. Since 2017, he has been a Full Professor with the Signals, Systems, and Radiocommunications Department, Universidad Politécnica de Madrid. His research interests include hardware design for radar systems, radar signal processing, and broadband digital receivers for radar and spectrum surveillance applications. Dr. Grajal was the co-recipient of the 2013 EuCAP Best Antenna Design Paper Award.